IEEE Access
practical innovations : open solutions

Received December 12, 2012, accepted April 9, 2013, published May 10, 2013.

Digital Object Identifier 10.1109/ACCESS.2013.2259134

Efficient, High Directivity, Large Front-to-Back-Ratio, Electrically Small, Near-Field-Resonant-Parasitic Antenna

MING-CHUN TANG (Student Member, IEEE)[1,2] AND RICHARD W. ZIOLKOWSKI (Fellow, IEEE)[3]

[1]Institute of Applied Physics, University of Electronic Science and Technology of China, Chengdu 610054, China
[2]College of Communication Engineering, Chongqing University, Chongqing 400044, China
[3]Department of Electrical and Computer Engineering, University of Arizona, Tucson, AZ 85721, USA

Corresponding author: R. W. Ziolkowski (ziolkowski@ece.arizona.edu)

ABSTRACT Enhancements of the directivity and front-to-back ratio (FTBR) of a metamaterial-inspired electrically small, linearly polarized, coaxially-fed Egyptian axe dipole antenna are considered. They are accomplished with a particular augmentation of the original near-field-resonant-parasitic (NFRP) antenna with an additional NFRP element, a small disc conductor modified with two meanderline-shaped slots. The entire system is evaluated numerically with two independent computational electromagnetics simulators. The optimized results demonstrate an electrically small antenna (i.e., $ka < 1.0$) with a reasonably low profile (i.e., height $\sim \lambda/10$) that improves the directivity from 1.77 to 6.32 dB, increases the FTBR from 0 to > 20 dB, and maintains large half-power beamwidths, while having a radiation efficiency over 80% with nearly complete matching to a 50 Ω source.

INDEX TERMS Directivity, efficiency, electrically small antennas, front-to-back ratio, metamaterial-inspired antennas, parasitic elements.

I. INTRODUCTION

Electrically small antennas (ESAs) have gained much attention and have been extensively studied for a variety of wireless applications. They enable the compact sizes preferred for mobile platform designs. On the other hand, because of their small electrical sizes, their directivities are small and near to those obtained from similar sized electric or magnetic dipoles. Moreover, their front-to-back ratio (FTBR) values are basically unity. It would be of significant practical benefit to many wireless applications to have ESA designs with interesting directivity and FTBR properties.

One of the recent approaches used to enhance the directivity of antennas has been to integrate known resonant radiators with electromagnetic band-gap (EBG) structures and other types of structured ground planes. Examples include: a CPW-fed cavity-backed slot antenna (EBG consisting of an array of rectangular patches, back plate mounted for additional directivity, 10.3 dB measured gain, 25 dB front-to-back ratio (FTBR), 85% overall efficiency with $ka = 6.66$ at 2.45 GHz) [1], where a is the radius of the smallest sphere that completely encloses the antenna at the operational frequency, f_0, and $k = 2\pi/\lambda_0 = 2\pi f_0/c$ is the free space wave number; an LTCC-patch antenna (mushroom EBG reflector, 4.8 dB measured boresight gain, 22 dB FTBR, 82% overall efficiency at 1575.42 MHz with $ka = 7.00$) [2]; a microstrip patch antenna (spiral-like unit cell EBG, 5.8 dB measured directivity, ∼12 dB FTBR, 95% measured overall efficiency at 2.4 GHz with $ka = 3.20$) [3], and a metamaterial-inspired electrically small antenna (degenerate band edge-based ground plane, 6.9 dB broadside gain, 95% overall efficiency at 2.59 GHz with $ka = 1.95$) [4].

While the performance characteristics of all of these antennas are admirable, their structured ground planes are nontrivial, not electrically small, and their integration with a radiating element requires a nontrivial design process. Another possibility is the super-directive, end-fire array approach [5]–[8]. By including a driven or parasitic twin in the very near-field of a driven ESA, large directivities can be obtained from such a two-element array. In this paper, we explore a related concept to achieve similar performance characteristics with a low-profile, metamaterial-inspired ESA system. In particular, we augment a near-field resonant parasitic (NFRP) ESA with an additional electrically small NFRP element—a slot-modified, conducting disc. The image of the NFRP ESA in the disc

acts as the second array element to achieve a high directivity, reasonably low profile system. Furthermore, by tuning the resonance characteristics of the parasitic disc, the pattern and associated FTBR values are managed.

The paper is organized as follows. In Section II, the coaxially-fed, linearly polarized, low profile, Egyptian axe dipole (EAD) NFRP ESA used in this paper is introduced. This EAD antenna is integrated with an electrically small, slot-modified, conducting disc in Section III. The combined system is comprehensively studied and its performance characteristics are obtained numerically with two independent computational electromagnetics simulation tools. It will be shown that the optimized system is significantly simpler than the EBG-augmented antenna designs, but still produces similar performance characteristics. Comprehensive comparisons between the proposed parasitic-augmented EAD antenna system and related systems, including a representative patch antenna, are given in Section IV. Finally, conclusions are discussed in Section V.

We will use the term electrically small to mean: $ka \leq 1.0$. To emphasize the ability to achieve an electrically small, high directivity antenna at low frequencies, we selected 300 MHz (1.0 m free space wavelength) as the frequency for this design effort. All of the numerical simulations and optimizations were carried out using both the frequency domain ANSYS/ANSOFT High Frequency Structure Simulator (HFSS) [9] and the time domain CST Microwave Studio (MWS) tool sets [10]. Their application to this problem is summarized in Appendix I. Details of an equivalent dipole model introduced in Section III to explain the properties of the actual parasitic-augmented EAD antenna system are discussed in Appendix II. All of the analytical calculations were performed in MatLab. An $\exp[+j(2\pi f)t]$ time dependence is assumed and suppressed throughout.

II. EGYPTIAN AXE DIPOLE ANTENNA

We selected the electrically small Egyptian axe dipole (EAD) antenna as the primary radiating element. While a version of the EAD ESA was first introduced to achieve an electrically small, planar Huygens source [11], it has been subsequently used to achieve electrically small, planar multifrequency and circular polarized antennas [12]–[14], and broad bandwidth non-Foster antennas [15], [16]. As with other metamaterial-inspired NFRP ESAs [12], the EAD antenna is nearly completely matched to a 50 Ω source (by choice) with no matching element and exhibits a high overall efficiency.

The low-profile EAD antenna used in the present study is shown in Fig. 1(a) and (b). Its dimensions are given in Table 1(a). The EAD was designed to be fabricated with the 2.5 mm, 0.5 oz copper (17 μm thick), Rogers TMM4 board material, which has a relative permittivity $\varepsilon_r = 4.5$, relative permeability $\mu_r = 1.0$ and a dielectric loss tangent equal to 0.002. The copper is modeled in all cases with its known parameters: $\varepsilon_r = 1.0$, $\mu_r = 0.999991$ and bulk conductivity $\sigma = 5.8 \times 10^7$ S/m. The HFSS-predicted resonance frequency is 300 MHz, giving $ka = 0.46$. At that frequency, the radiation

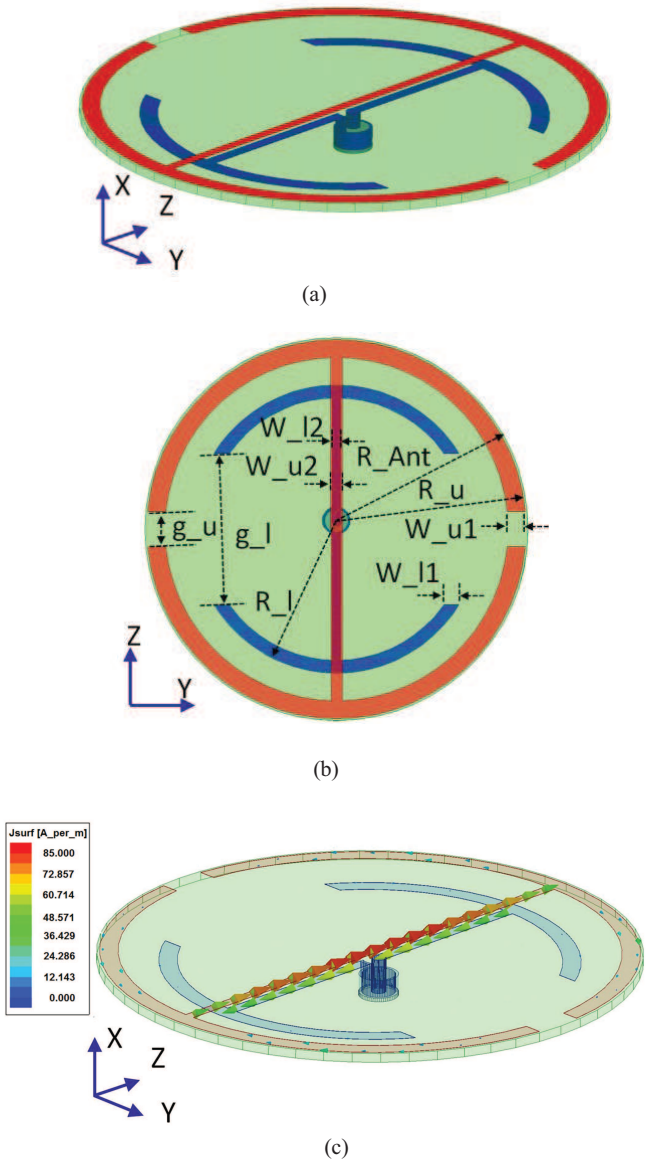

FIGURE 1. The EAD antenna. (a) 3D isometric view, (b) 2D top view with dimensions, and (c) current densities at the resonance frequency.

efficiency (total power radiated to total accepted power) is $RE = 90.86\%$. As shown in Fig. 2, it is nearly completely matched to the 50 Ω source, i.e., $|S_{11}| = -25.99$ dB, giving an overall efficiency (total power radiated to total input power) OE = 90.63%. The −10dB bandwidth is 3.22 MHz (∼1.07% fractional bandwidth); the half-power bandwidth is 10.00 MHz (∼3.33% fractional bandwidth). As with most NFRP designs [11], the currents at the resonance frequency, as shown in Fig. 1(c), are mainly on the NFRP element. These performance characteristics were verified independently with the CST MWS tools.

However, because it is electrically small, the EAD antenna simply exhibits the directivity associated with a small dipole antenna. This is illustrated with the E- and H-plane patterns at the resonance frequency shown in Fig. 3(a) and (b). The maximum directivity is 1.77 dB and the FTBR = 0 dB.

TABLE 1. The optimized parameters of the EAD antennas integrated with the meandered-slot modified, finite ground plane (mm).

(a) EAD Antenna Alone

$R\_u = 73$	$g\_u = 14.1$	$W\_u1 = 5$	$W\_u2 = 2.97$	$R\_l = 57$
$g\_l = 60$	$W\_l1 = 5.95$	$W\_l2 = 3.5$	$R\_Ant = 73.8$	

(b) EAD Antenna With Parasitic Disc, $H = 50$ mm

$R\_u = 75.0$	$g\_u = 14.0$	$W\_u1 = 7.0$	$W\_u2 = 4.6$	$R\_l = 53.0$
$g\_l = 60.0$	$W\_l1 = 6.24$	$W\_l2 = 4.0$	$R = 10.4$	$R1 = 16.0$
$R2 = 26.0$	$W = 8.0$	$W1 = 11.5$	$W2 = 16.9$	$W3 = 0.9$
$L1 = 32.0$	$L2 = 12.0$	$L3 = 24.3$	$L4 = 10.5$	

(c) EAD Antenna With Parasitic Disc, $H = 60$ mm

$R\_u = 75.0$	$g\_u = 14.0$	$W\_u1 = 7.0$	$W\_u2 = 4.53$	$R\_l = 53.0$
$g\_l = 60.0$	$W\_l1 = 6.24$	$W\_l2 = 4.5$	$R = 10.4$	$R1 = 16.0$
$R2 = 26.0$	$W = 8.0$	$W1 = 12.0$	$W2 = 17.4$	$W3 = 0.9$
$L1 = 31.8$	$L2 = 12.0$	$L3 = 24.3$	$L4 = 10.47$	

(d) EAD Antenna With Parasitic Disc, $H = 100$ mm

$R\_u = 75.0$	$g\_u = 14.0$	$W\_u1 = 7.0$	$W\_u2 = 4.48$	$R\_l = 57.0$
$g\_l = 60.0$	$W\_l1 = 5.95$	$W\_l2 = 3.5$	$R = 10.4$	$R1 = 16.0$
$R2 = 26.0$	$W = 8.0$	$W1 = 14.25$	$W2 = 19.25$	$W3 = 0.9$
$L1 = 31.8$	$L2 = 12.0$	$L3 = 24.3$	$L4 = 10.5$	

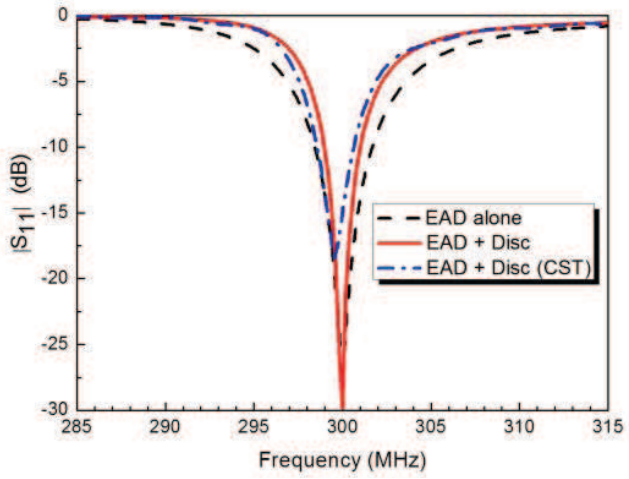

FIGURE 2. The HFSS- and CST-predicted $|S_{11}|$ values versus the frequency for the coax-fed EAD integrated with the slot-modified, parasitic copper disc when their separation distance $H = 100$ mm $= \lambda_0/10$.

It has been demonstrated previously that its directivity can be increased by combining it with other radiating objects. For instance, its integration with an EBG-structured ground plane produced a 4.36 dB directivity and a 4.88 dB FTBR [14]. On the other hand, its integration with a magnetic dipole [11] increased its FTBR (from 0 dB to 17.1 dB) and its directivity (4.5 dB) to near the theoretical maximum ($2 \times 1.5 = 3.0$ or 4.77 dB). Nonetheless, even higher directivities and larger FTBRs would be desirable for many wireless applications.

III. EAD AUGMENTED WITH A SLOT-MODIFIED, PARASITIC CONDUCTING DISC

Because it was shown [17] that slots in the ground plane of a microstrip patch antenna can be designed to mitigate the

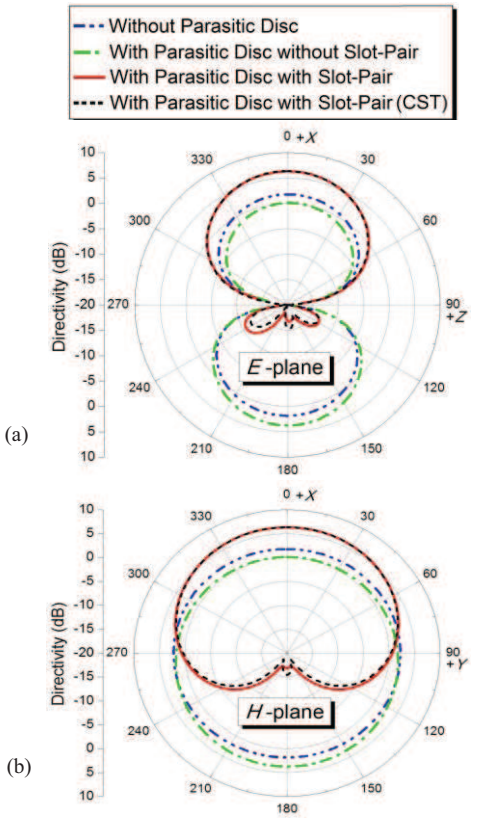

FIGURE 3. Comparisons of the directivity patterns in the *E*- and *H*-planes when $H = 100$ mm when the EAD is alone and when it is augmented with the slot-modified parasitic copper disc.

formation of its backlobe, it was decided to try a similar approach with the EAD antenna. Fig. 4 shows the coax-fed EAD antenna integrated with a slot-modified conducting disc. The disc has two meanderline slots cut in it. It is oriented parallel to the EAD elements while the centerlines of the slots are oriented orthogonal to the axis of those elements. The disc is not connected to the coax-feed line and, thus, acts as a parasitic element. The slots present a means to tune its resonance to match that of the EAD antenna. Because they are oriented orthogonal to the axis of the EAD antenna, the slots can be resonantly tuned to create the amplitudes and phases of the currents in the parasitic disc required to achieve the desired large FTBR values (see Appendix II). The inside edges of the slots are specially designed to conform to the coax-feedline shape. The radius of the EAD antenna and the parasitic disc were specified to be $R\_Ant = 75.8$ mm and $R\_GND = 150$ mm, respectively. This gives $ka_{ANT} = 0.48$ and $ka_{GND} = 0.94$. Both the driven antenna and the overall system are thus electrically small. The slot-modified disc was taken to be copper and to have a 1.0 mm thickness. The height of the EAD antenna structure over the ground plane, H, is specifically the distance of separation between the bottom of the EAD antenna and the top of the slot-modified parasitic disc. For a specific H, the EAD and disc parameters were optimized to obtain nearly complete matching to the 50 Ω source. Three low-profile cases: $H = 50$ mm ($\lambda_0/20$), 60 mm

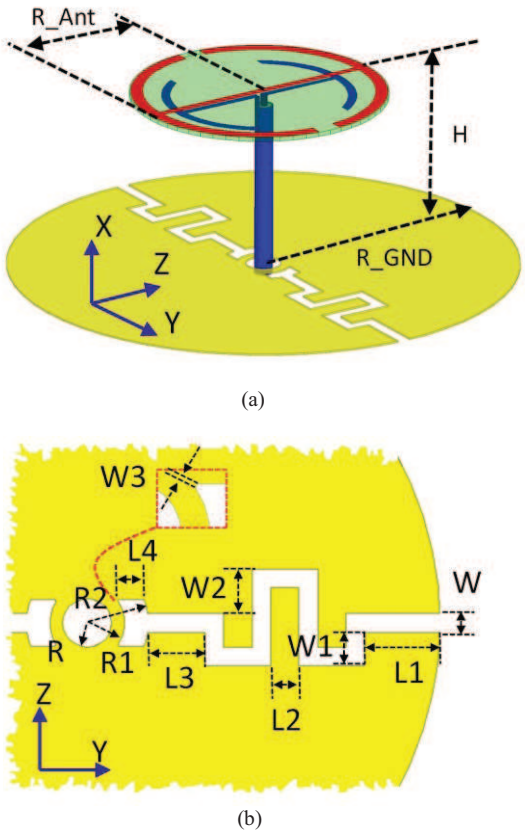

FIGURE 4. The EAD antenna integrated with the slot-modified, parasitic copper disc. (a) 3D view, and (b) zoom-in view of one of the meanderline slots and its design parameters.

($\lambda_0/16.67$), 100 mm ($\lambda_0/10$), are reported here. The last one still remains relatively low-profile and maintains the electrically small nature of the system while being a simple value to remember. The $H = 100$ mm case will be used below to illustrate various aspects of such designs and how they impact the resulting performance characteristics.

The specific dimensions for all three cases are given in Table 1(b)–(d). Note that W3 indicates the length of the chamfer on the end of each meanderline slot. The presence of the chamfer enabled additional fine tuning of the amplitudes and phases of the currents produced by the slots. The predicted performance characteristics for each case are given in Table 2. With the design parameter Tables, the consequences of the choices of the system design parameters become apparent. Furthermore, to illustrate these results in the neighborhood of the resonance frequency, both the HFSS- and CST-predicted $|S_{11}|$ values as functions of the frequency for the $H = 100$ mm system are illustrated in Fig. 2. They agree very well and show that this $ka = 0.94$ system is nearly completely impedance matched to a 50 Ω source at 300 MHz without any additional matching elements. The simulation results display a −10 dB fractional bandwidth of 0.67% and a half-power fractional bandwidth of 2.07%. The corresponding directivity patterns for the EAD antenna when it is augmented with a parasitic copper disc, having and not having two meanderline slots, are presented in Fig. 3 along with those of the EAD-alone results. The agreement of the HFSS- and CST-predicted results is again very good. The enhancement of the directivity and FTBR properties are immediately apparent only when the additional parasitic element with the two meanderline slots is present. In particular, the corresponding performance characteristics exceed all of the initial design criteria: RE > 80%, FTBR > 20 dB, and directivity > 6.0 dB, confirming the advantage of the proposed design.

TABLE 2. Performance characteristics of the EAD antenna augmented with the slot-modified parasitic copper disc.

Properties at 300 MHz	H = 50 mm ($0.05\lambda_0$)	H = 60 mm ($0.06\lambda_0$)	H = 100 mm ($0.10\lambda_0$)	H = 100 mm (CST)
$\|S_{11}\|$ (dB)	−25.06	−29.84	−29.82	−18.74
−10 dB impedance bandwidth (%)	0.4	0.4	0.67	0.69
Peak directivity (dB)	6.17	6.29	6.32	6.33
E-plane HPBW	74.5°	75.0°	76.0°	74.4°
H- plane HPBW	134°	135°	138°	134°
Radiation efficiency (%)	78.9	80.97	86.87	86.53
Front-to-back ratio (dB)	16.15	20.11	23.16	21.8
Total length (mm) of one edge of the slot	231.08 ($0.23\lambda_0$)	234.08 ($0.235\lambda_0$)	246.79 ($0.245\lambda_0$)	246.79 ($0.245\lambda_0$)

Moreover, from Table 2 and the pattern comparisons given in Fig. 3, one finds at the resonance frequency, 300 MHz, for instance, that the maximum directivity is enhanced from 1.77 dB for the EAD alone to 6.32 dB (a 4.55 dB improvement) for the $H = 100$ mm case. The FBTR value is also increased from 0 dB to greater than 20 dB (23.16 dB). The half-power beamwidth is 76° in the E-plane and 138° in the H-plane. These pattern improvements occur with a radiation efficiency of 86.87%. However, note that the backlobes of the E-plane pattern are not symmetric. This is a result of the unbalanced feed structure of the EAD. As can be seen from Figs. 1(a) and 4(a), the center conductor of the coax connects to one arm of the driven element; the outer wall is connected to the other. The asymmetry is accentuated in this application because of the height of the EAD above the parasitic element. Also note that when the EAD is simply integrated with an unmodified parasitic copper disc, an actual degradation of its broadside directivity (in $+x$ direction) by 1.75 dB occurs. This response arises because the copper disc is electrically small and not resonant, i.e., $a_{GND} = 0.15\lambda_0$, and the height of the EAD above it is not optimized. As will be discussed in detail in Section IV, the image currents on the disc act as an electric dipole oriented in a direction opposite

to those on the EAD, which leads to the observed decrease when the separation distance is not optimal.

We note that the significant enhancement of the FTBR value when the meanderline slots are present, and no enhancement in their absence, suggests that the slot-modified parasitic copper disc is behaving more than a simple resonant reflector element. The latter interpretation would only explain its enhanced directivity behavior in the context of an effective two-element end-fire array. We find that when the slots are tuned to be in resonance with the EAD antenna, the disc also helps stabilize the pattern so its null occurs opposite to it maximum.

To elucidate this additional physics, the current distributions at the resonance frequency, 300 MHz, on the electrically small EAD antenna augmented with the slot-modified parasitic copper disc when $H = 100$ mm are shown in Figs. 5 and 6. As observed in Fig. 5(b), the currents on the EAD antenna components have been altered by the presence of the parasitic disc. Different from that in Fig. 1(c), the currents on the driven element are much larger than those on the parasitic element. Since they are in opposite directions and are extremely close to one another, their combination produces a dipole field oriented relative to the current direction on the driven element. Then, as shown in Figs. 5(c) and 6(a) and (b), the largest magnitudes of the currents present on the top side of the disc occur on the edges of the meanderline slots near the coax-feedline hole. The currents on the bottom side of the disc are essentially identical to those on the top side. Nonetheless, all of the rest of the currents away from the coax-feedline hole have a strong net orientation in the direction opposite to the net current on the EAD antenna elements. Thus, the currents away from the hole on the parasitic copper disc cause it to act as a resonant reflector element in an effective two-element near-field Yagi configuration [5]–[8], causing the observed directivity enhancements. Additionally, however, because the parasitic disc is in the near-field of the EAD antenna, the coupling of the EAD-generated fields to its slots is quite strong. Thus, the currents associated with the meanderline slots also significantly impact the radiation patterns.

As is shown in Fig. 6(c), the current pathways along the meanderline slots are in opposite directions along their upper and lower edges. Moreover, they have opposite orientations on both sides of the coax-feedline, i.e., with respect to the z-axis. Thus, their effects on the radiation patterns cancel out. On the other hand, the very strong z-oriented currents on the inside edges of the slots are in the same direction on both the top and bottom sides of the parasitic disc. This is affected by the phase differences resulting from the effective length of one side of each of the slots being close to a quarter-wavelength. Thus, the fields these elements generate superimpose constructively. These fields are responsible for the enhancement of the FBTR. The fields radiated by these slot edges are further impacted by the pair-wise combinations of the different magnitude z-oriented excitations distributed at various positions along the meanderline slots determined by the slot geometry parameters. Parameter studies of the shapes

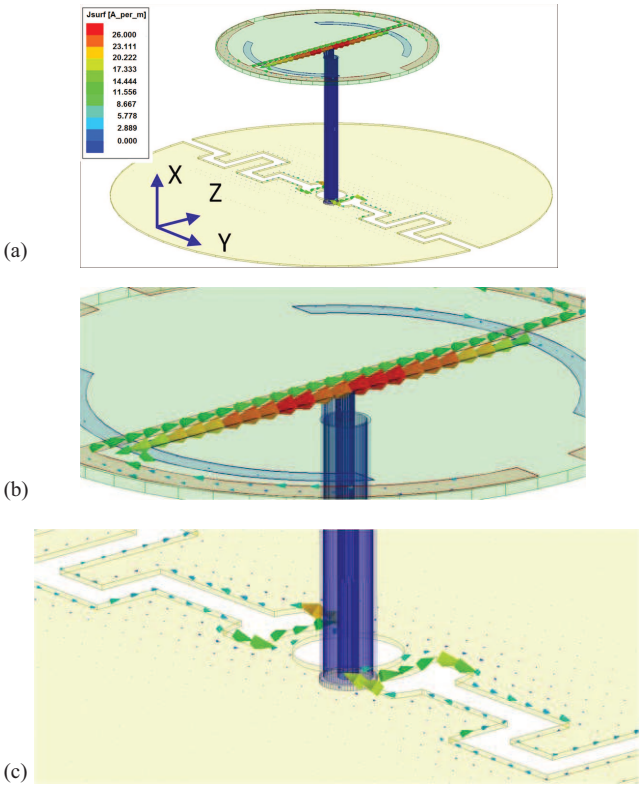

FIGURE 5. Current densities on the EAD antenna augmented with the slot-modified parasitic copper disc when $H = 100$ mm. (a) Isometric view of the entire structure, (b) zoom-in view of the driven and NFRP elements of the EAD antenna, and (c) zoom-in of the two meanderline slots near their inside edges.

of the ends of the slots, to maximize their magnitudes and their phases relative to the net EAD and parasitic disc currents led to the final design shown in Fig. 4(b), their parameters given in Table 1, and to the resulting optimized FTBR values.

These current behaviors lead to the four-element, infinitesimal dipole array model shown in Fig. 7 to help explain the performance characteristics of the entire antenna system. Antenna 1 represents the EAD currents, antenna 2 represents the ''reflector'' currents, and antennas 3 and 4 represent the inside slot edge currents. As shown in Appendix II, this four-element array reproduces the desired cartoid-like radiation patterns, which lead to the desired enhanced FTBR values.

To further understand the phase relationships between the net currents associated with the EAD antenna, the reflector effect of the parasitic copper disc, and the inside edges of the meanderline slots, we plot in Fig. 8 the magnitude of the E-field distributions in the near field of the entire system for different phase values of the driven excitation over a half-period. The fields associated with the EAD are largest where the displacement currents exist in the gaps of the driven and NFRP elements. The fields around the parasitic copper disc are largest along the z-oriented edges of the meanderline slots, particularly at their outside edges. One can clearly see how the fields directly from the EAD and

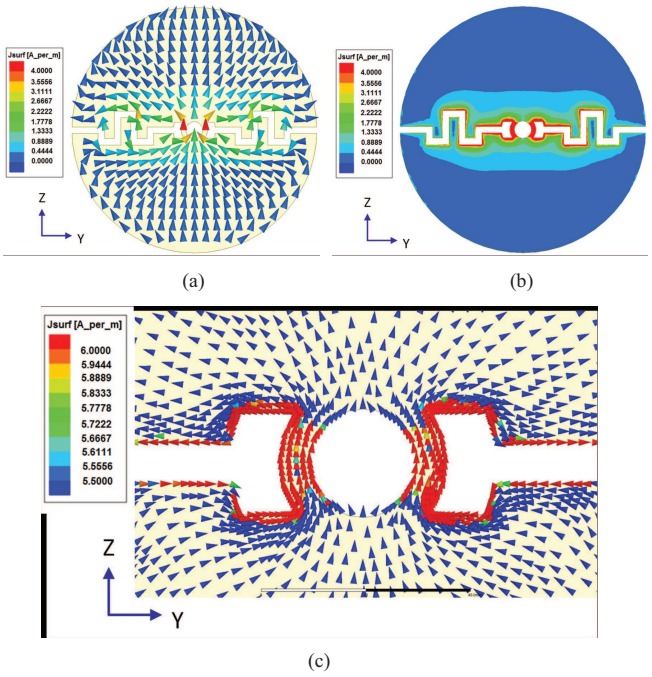

FIGURE 6. Current density on the front surface of the slot-modified parasitic disc associated with the configuration shown in Fig. 5. (a) Vector distribution, (b) magnitude distribution, and (c) zoom-in near the inside edges of the meanderline slots. The current distribution on the back side is the mirror (with respect to the *z*-axis) of the front side.

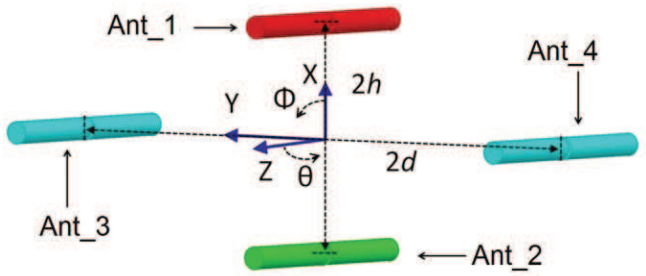

FIGURE 7. The effective four-element infinitesimal dipole array model.

from the slot-modified parasitic copper disc are out-of-phase with one another (especially in the $5\pi/12$ and $2\pi/3$ cases), which leads to the desired difference pattern in the backlobe direction and the enhanced FTBR value.

To determine the directivity bandwidth of the $H = 100$ mm design, the radiation efficiency, FTBR, directivity, gain, and realized gain values as functions of the frequency are shown in Fig. 9(a) and (b). It can be seen in these figures that the FTBR and realized gain values reach their peak values at the design frequency, 300 MHz. Moreover, one finds that the -3 dB realized gain bandwidth is from 297.3 MHz to 303.3 MHz, 6 MHz ($\sim$2.0% fractional bandwidth). On the other hand, the bandwidths of the directivity and gain are much broader and harder to stipulate given their frequency behaviors.

The design parameters and performance characteristics of the $H = 50$ mm and $H = 60$ mm cases were also given

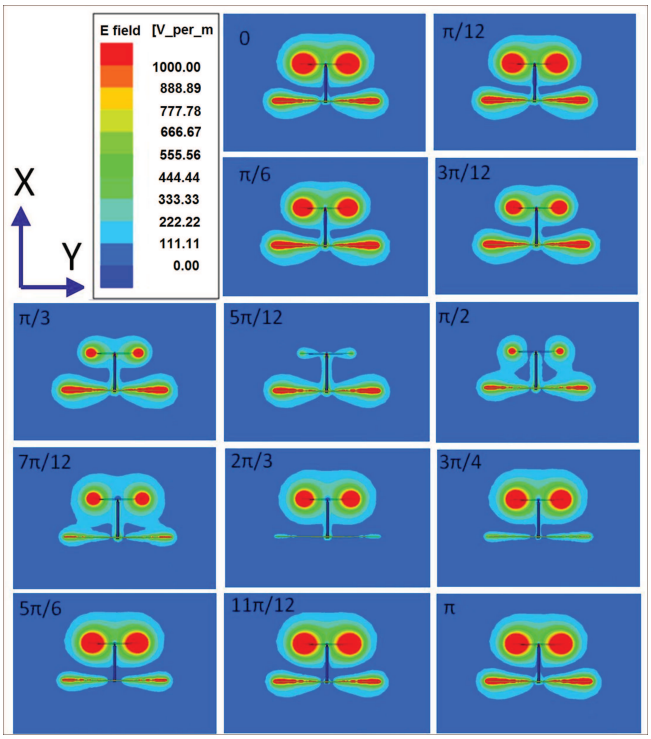

FIGURE 8. The near-field distributions of the magnitude of the *E*-field of the entire system over a half-period of the excitation.

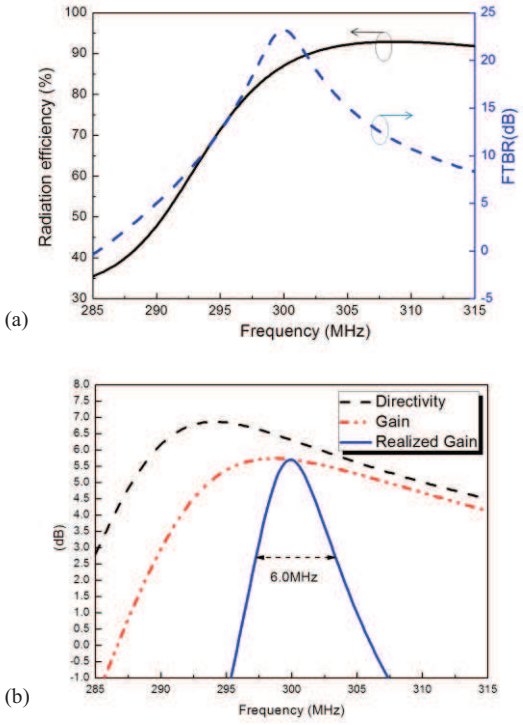

FIGURE 9. Directivity, FTBR, gain, and realized gain values as functions of the frequency for the EAD antenna augmented with the slot-modified parasitic copper disc when $H = 100$ mm.

in Tables 1 and 2. It is observed that as the height H of the EAD above the ground plane is decreased, the FTBR and

the radiation efficiency values decrease slightly, while the maximum directivities and pattern beamwidths vary little. The decrease in the radiation efficiency can be attributed to the closeness of the disc as a "reflector". Nonetheless, the values of the low-profile $H = 50$ mm case would be quite acceptable for a variety of wireless applications. Although the final system would not be electrically small, larger R_{GND} and H value cases were nonetheless considered. Their FTBR and radiation efficiency values are even greater than those given in Table 2. Furthermore, the results for smaller ground plane sizes were also obtained, e.g., for R_{GND} reduced to 100 mm, while $H = 50$ mm. It was found that the antenna system can also be nearly completely matched to the source ($|S_{11}| = -20.2578$ dB) with a high radiation efficiency (84.7%). However, the directivity and front-to-back ratio are only 2.57 dB and 1.22 dB, respectively, which are well below the desired values. As discussed in Appendix II, this behavior confirms that when the structured parasitic ground is not large enough, the phases and amplitudes of the currents on it cannot be adjusted to the requisite values. Even though the meanderline slot can be made large enough by forcing large deviations of the slots along the y-axis, there is too much of the parasitic copper disc removed and the current amplitudes cannot attain their necessary values.

IV. DISCUSSION

The performance characteristics of the slot-modified disc augmented EAD antenna system have been compared with several related structures. As a first example, we investigated the same EAD antenna augmented with an unmodified parasitic copper disc, as a reflector element at the fixed distance $H = 100$ mm. The simulation geometry is shown Fig. 10(a). The reflector radius was enlarged from 150 mm to 1100 mm; the directivity, FBTR, and radiation efficiency values were obtained. They are plotted as functions of the disc radius in Fig. 10(b) and (c). As is shown in Fig. 10(b), when the reflector is too small ($R\_GND < 210$ mm), it does not act as an "effective reflector". In particular, the FTBR values are negative in this radius range. In contrast, when the reflector is large enough ($R\_GND > 210$ mm), the directivity and FTBR values increase positively. When R_GND becomes 250 mm, the directivity equals the value, 6.32 dB, of our design. However, for even much larger radius values, the FTBR never exceeds 18 dB. On the other hand, the EAD and the reflector element combine to have a directivity approaching the theoretical maximum 9.22 dB for $R\_GND =$ 705 mm [5]–[8], Moreover, the radiation efficiency is always lower than 85% due to the oppositely oriented currents on the EAD antenna and on the metallic reflector.

The $|S_{11}|$ values when $R\_GND = 250$ mm give a 1.15 MHz -10 dB bandwidth (0.38% fractional bandwidth). The radiation efficiency is 74.71%. As shown in Fig. 10(d), the FTBR is 2.74 dB and the HPBW in the E- and H-planes are, respectively, 66° and 90°. The RE is 10% less and the FTBR is more than 20 dB less than the proposed design values, even though now $ka = 1.57$. Note that this also means the effective area of

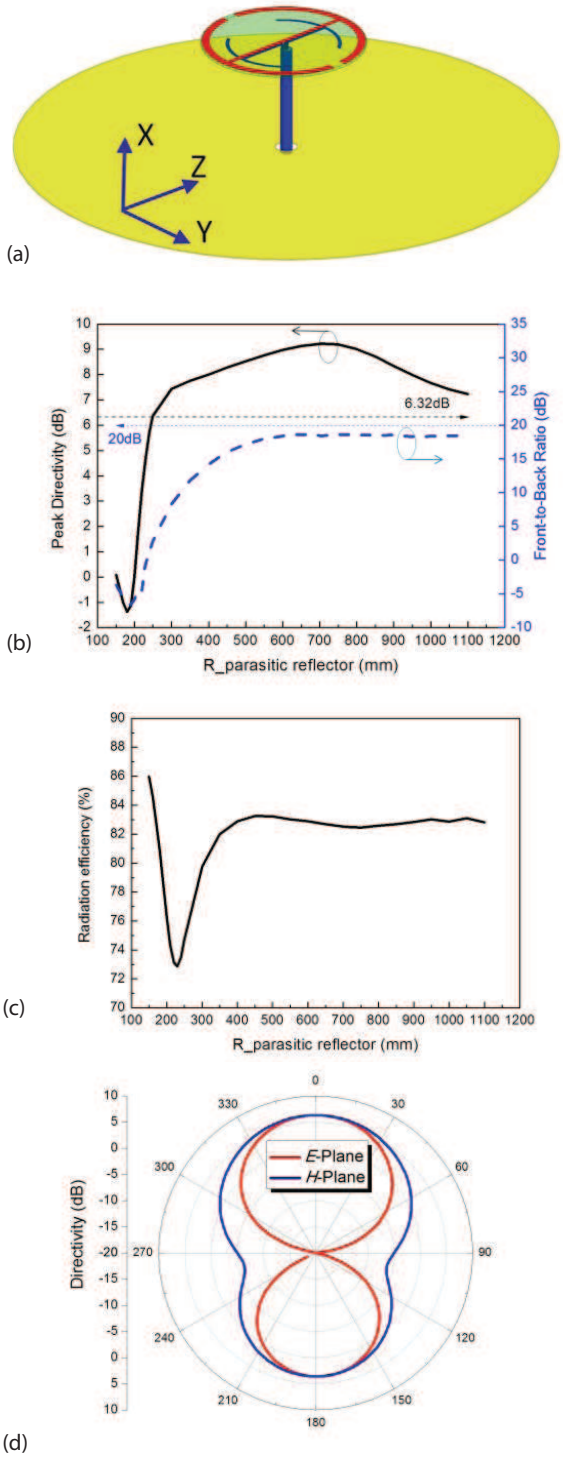

FIGURE 10. EAD antenna operating at 300 MHz augmented with an unmodified parasitic copper disc. (a) Isometric view; (b) the peak directivity and FTBR; and (c) radiation efficiency values as the radius of the disc is increased from 150 to 1100 mm; and (d) the *E*- and *H*-plane directivity patterns when $R\_GND = 250$ mm.

this system is about 2.8 times larger than the proposed design (i.e., recall that $D_{max} = (4\pi/\lambda^2)A_{eff}$).

We note that the super-directivity performance of the closely spaced two-element end-fire arrays reported in [5]–[8] produces a theoretical maximum directivity of

7.76 dB when those elements exhibit simple dipole behaviors and 9 dB if both electric and magnetic dipoles are included simultaneously. When losses are taken into account, the measured peak values are, of course, lower.

Following those investigations, we have considered as a second comparison example: an end-fire array consisting of two EAD antennas, one driven and the other acting as a parasitic element, in the two possible end-fire configurations shown in Fig. 11(a) and (b). In the vertical orientation, the maximum directivity values were obtained as the distance D between their centers was varied along the x-axis from $0.05\lambda_0$ to $0.3\lambda_0$. When the distance D was 125 mm, the maximum directivity in the $+x$ direction, 6.35 dB, was obtained for the resonance frequency 297.6 MHz, a 2.4 MHz shift due to the coupling of the two elements. For this frequency, its performance characteristics are: $|S_{11}| = -19.48$ dB, RE = 70.86%, FTBR = 13.16 dB and HPBW = 73.9° and 129.3° in the E- and H-planes, respectively. The 3D directivity pattern at the resonance frequency is shown in Fig. 11(c).

In the same manner, the horizontal orientation was examined with D changing from $0.16\lambda_0$ to $0.3\lambda_0$ along the y-axis. The maximum directivity, 6.40 dB in the $+y$ direction, was obtained for D = 225 mm for the resonance frequency 297.0 MHz, a 3.0 MHz shift. Its performance characteristics at resonance are: $|S_{11}| = -16.18$ dB, RE = 81.81%, FTBR = 5.65 dB and HPBW = 75.5° and 114.5° in the E- and H-planes, respectively. The 3D directivity pattern at the resonance frequency is shown in Fig. 11(d); the presence of nontrivial backlobes is rather noticeable. While both explicit two-element EAD array cases produced directivities on the same order as the proposed design, the latter outperforms them and produces, in particular, significantly lower FTBR values.

Finally, we designed an offset coax-fed, circular microstrip patch antenna operating near 300 MHz with the height $H = 100$ mm and matched to a 50 Ω source as a third comparison example. Its preliminary design at 300 MHz was obtained using well-known formulas [18]; it was then refined with HFSS simulations.

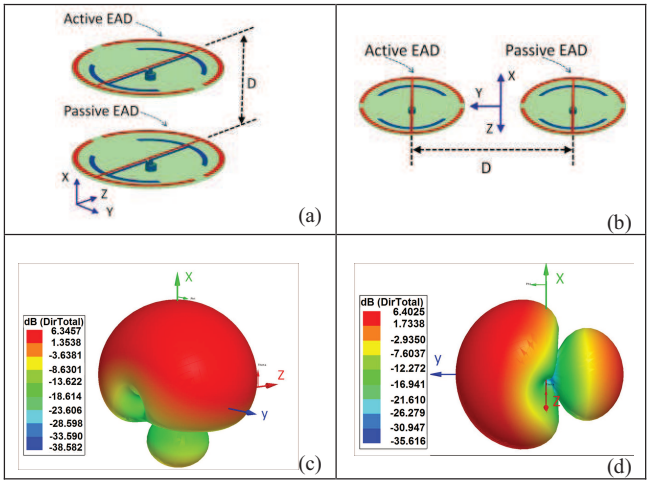

FIGURE 11. End-fire array configurations using two EAD elements. (a) Vertical orientation, (b) horizontal orientation, and the 3D directivity pattern at resonance for the (c) vertical orientation and (d) horizontal orientation.

The HFSS model is shown in Fig. 12(a). Several patch and ground plane radii were studied. With the patch radius being $R\_1 = 112$ mm and the Rogers TMM4 substrate height being $H = 100$ mm ($0.212\lambda_g$), Fig. 12(b) shows the directivity and FTBR values as functions of the ground plane radius R_2. The smallest ground plane which produces comparable values to our proposed design is $a = 299.21$ mm. The antenna is operating at 300 MHz with a −10 dB bandwidth of 40.58 MHz (fractional bandwidth 13.53%). The peak directivity is 6.33 dB; RE = 99.06%; and FTBR = 16.42 dB. Plots of the E- and H-plane directivity patterns are given in Fig. 12(c). The HPBW values in the E- and H-planes are, respectively, 93.2° and 100°. The electrical size is $ka = 1.89$, which is double that of our proposed design. Thus, the effective area of this comparison system is 4.0 times larger than the proposed design. While the other performance characteristics are similar to those of the proposed design, the FTBR values could not be improved larger than 18 dB. Notice that because the height of substrate is so large in this unbalanced feeding system, the maximum directivity goes away slightly from broadside direction when the ground plane radius is small. Also notice from Fig. 12(b) that the directivity values become comparable to our design only for several much larger values of the ground plane radius. On the other hand, around $R\_2 = 800$ mm or 1600 mm, the peak directivity values are actually in the opposite direction, which is why there are two noticeable minima in the figure.

V. HIGH BROADSIDE DIRECTIVITY ARRAY

In addition to considering the end-fire and side-by-side driven-parasitic configurations, the use of the high directivity single element in a two-element driven array was also investigated. The configuration is shown in Fig. 13. Without any changes to the original elements, it was found at 300 MHz that the maximum broadside (along the $+x$ axis) directivity, 9.65 dB, occurred for the center-to-center distance $d = 675$ mm. Since $R\_GND = 150$ mm, this was a 375 mm $< \lambda_0/2$ separation between the edges of the discs. At this distance, it was found that the mutual coupling $|S_{21}| = -20.51$ dB; RE = 90.28% giving the gain G = 9.21 dB; the sidelobe level maximum was −9.73 dB; and the E- and H-plane 3 dB beamwidths were, 78° and 44°, respectively. The directivity was slightly more than the anticipated 3 dB improvement, but the FTBR was only 15.8 dB. It was found that this lower FTBR value was due, despite its already low value, to mutual coupling effects between the two antennas.

In an attempt to improve its performance, several aspects of the individual elements were varied. It was determined that the transverse variations in the meanderline, along which the

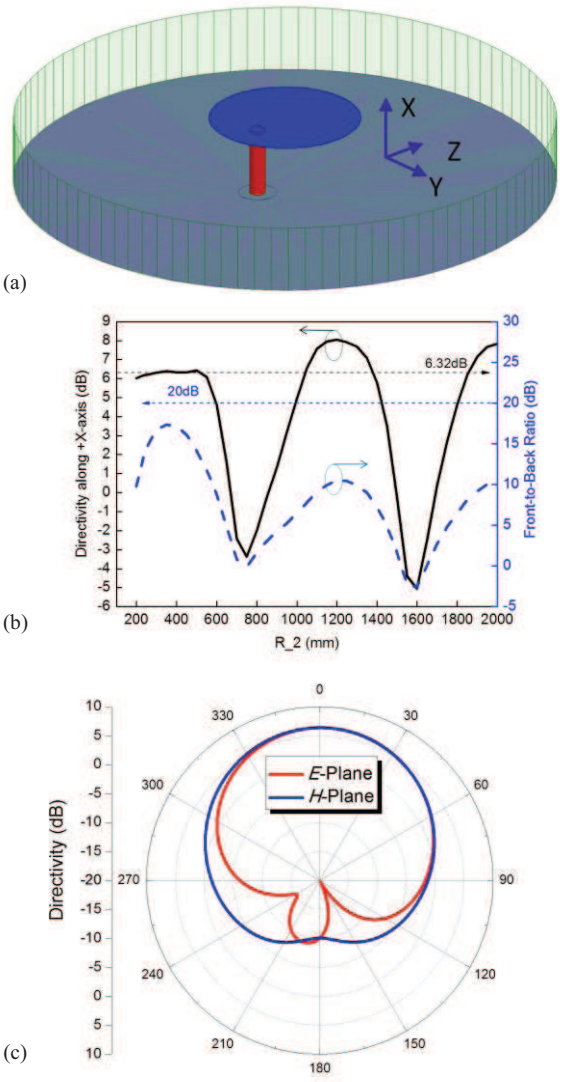

FIGURE 12. Comparison coax-fed circular patch antenna. (a) Isometric view, (b) peak directivity and FTBR values as functions of the ground plane radius, and (c) *E*- and *H*-plane directivity patterns when the ground plane radius is 299.21 mm.

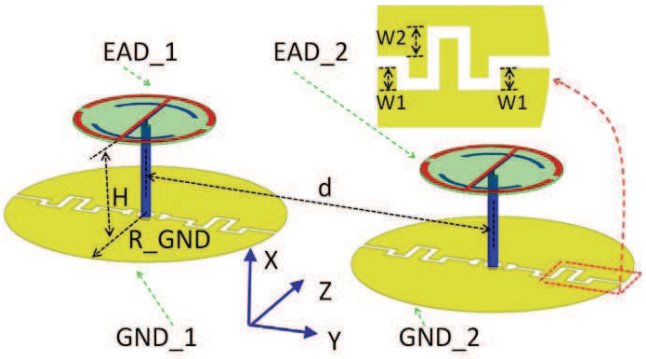

FIGURE 13. The two-element array configuration formed by two parasitic disc augmented EAD antennas, each operating at the center frequency of 300 MHz with $H = 100$ mm, $R\_GND = 150$ mm, $R\_Ant = 75$ mm and the separation distance d.

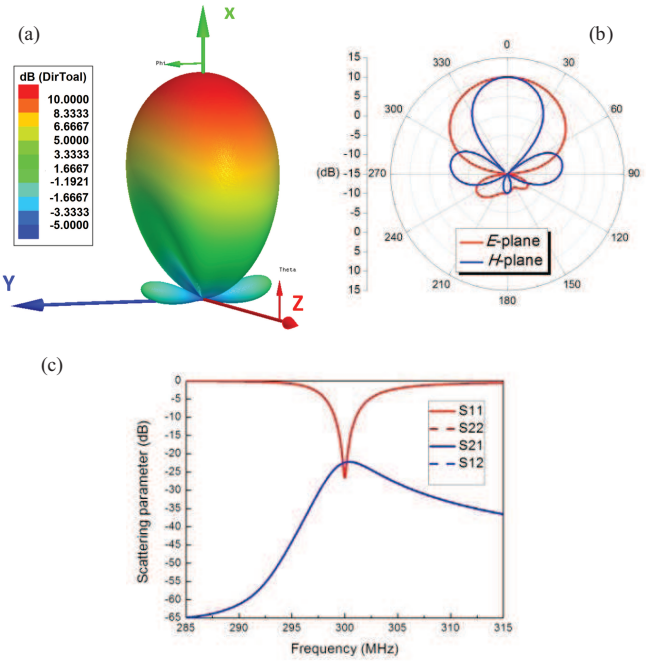

FIGURE 14. The optimized two-element parasitic ground plane-augmented EAD array. (a) Simulated 3D directivity radiation pattern, (b) the corresponding *E*- and *H*-plane patterns, and (c) the S-parameters.

currents act as small dipoles and produce the undesired back radiation, had the largest impact. The best FTBR value was obtained for $W2 - W1 = 2.0$ mm, i.e., because the broadside directivity and the radiation efficiency have a mutual tradeoff effect, one finds that changing the lengths of the slots to minimize their radiation effects is an effective way to adjust these performance characteristics to recover the maximum possible values. Note that with $d = 675$ mm, the entire two-element array is confined within a sphere whose radius $a < 0.5\lambda_0$. With $W2 - W1 = 2.0$ mm, the simulated performance characteristics are summarized in Fig. 14. The 3D directivity pattern and the corresponding E- and H-plane patterns are shown, respectively, in Fig. 14(a) and (b). The array produces a very desirable 9.98 dB broadside directivity, −10.57 dB side lobe level, and 20.03 dB FTBR value with RE = 88.19%. In Fig. 14(c), both elements are well-matched to their 50 Ω sources with the minimum values $|S_{11}|_{min} = |S_{22}|_{min} = -26.70$ dB, at the specified 300 MHz operational frequency. At that frequency, the maximum mutual coupling values are: $|S_{21}|_{max} = |S_{12}|_{max} = -22.42$ dB. Both elements have a −10 dB fractional bandwidth of 0.66%, and a half-power fractional bandwidth of 2.23%. The half-power beamwidths in the *E*- and *H*-plane remain around 78° and 44°, respectively.

VI. CONCLUSIONS

An Egyptian axe dipole antenna, a NFRP ESA, was integrated with a slot-modified parasitic copper disc to obtain an electrically small system ($ka < 1$) with a reasonably

low-profile ($\lambda_0/10$) that has a high directivity and a large FTBR. In particular, by optimizing its design parameters, the directivity of one such NFRP ESA was enhanced 4.55 dB, up to 6.32 dB, with a significantly increased FTBR, from 0 dB to 23.16 dB, while also obtaining a large half-power beamwidth. Its radiation efficiency was high at 86.87%. A four-element dipole array analytical model was introduced to help guide the characterization of its radiation properties, especially how such a design could achieve a large FTBR value. This model provided confirmation that the parasitic disc acted more than a simple reflector element; it helped identify the presence of the currents along the inside edges of the slots and their impact on the FTBR. The proposed system was compared to several existing approaches, such as a reflector-backed EAD, a closely packed two element EAD array and a conventional coax-fed circular patch antenna. On the other hand, with both elements being driven and optimized to minimize their mutual coupling effect, the two-element array produced a 9.98 dB broadside directivity with RE = 88.19% and FTBR = 20.03 dB.

Our proposed high directivity ESA was demonstrated to have several distinct performance advantages. While we emphasized the modification of an EAD antenna with the resonant slot-modified parasitic conducting disc to enhance its directivity and FTBR values, the same approach is applicable to any dipole-like ESA. On the other hand, note that the reported designs have narrow impedance bandwidths. Nonetheless, there are numerous narrow bandwidth applications for such ESAs, particularly given the simplicity and compactness of their designs, their potential low-cost fabrication and superior performance characteristics. These include, for example, wireless power transfer (WPT), wireless sensor and GPS systems.

APPENDIX I. COMPUTATIONAL EM TOOLS

The simulations performed for this paper were accomplished with both ANSYS-ANSOFT HFSS and CST MWS. As shown in several of the references, we have had good success with experimental confirmation of our HFSS simulations for a variety of electrically small metamaterial-based and metamaterial-inspired antennas. Similar success with CST MWS has been reported by a variety of international groups. The HFSS tool set uses the Finite Element Method (FEM) in the frequency domain. We used here the time domain the Finite Integration Technique (FIT) tools in the CST MWS tool set.

We have found the HFSS tools to be cost-effective and accurate for narrow bandwidth, highly resonant antennas, such as those reported in this paper. We have performed convergence testing of the CST simulations involving more than several million hexahedral mesh cells and several days of run times to compute the final antenna design. We use the transient solver to calculate the model, with the frequency range [250 MHz, 350 MHz] and with a required steady state accuracy of −30.0 dB. Based on these convergence study results using different mesh cell numbers, which are summarized in Table 3, the final results have little variation with increasing numbers of mesh elements and agree very well with those obtained with HFSS. Additionally, any small variations in the CST numerical results from one mesh size to another are quite acceptable for such a time domain computational method and for its particular adaptive mesh scheme. Note that the simulation times to finish these time domain simulations are quite large. In contrast, typical run times for a corresponding HFSS simulation with the frequency range from 250 MHz to 350 MHz with the step 0.2 MHz were generally around 3 hours. We used a server computer with 2 Intel(R) Xeon (R) CPUs, 144GB RAM, and a 64-bit operating system to obtain all of these results. The results given in the main text arose from the Case 4 simulations.

TABLE 3. CST MWS convergence and accuracy test results.

Category	Case 1	Case 2	Case 3	Case 4
Hexahedral mesh cell number	1,797,120	2,356,640	3,365,856	3,613,302
Total simulation time	2 h, 54 m	4 h, 06 m	8 h,55 m	10 h, 05 m
Resonance freq. f_{res} (MHz)	300.04	299.87	299.60	299.57
$\lvert S_{11}(f_{res})\rvert_{min}$ (dB)	−19.98	−19.64	−18.90	−18.74
−10 dB impedance bandwidth (%)	0.73	0.72	0.70	0.69
Peak directivity (dB)	6.31	6.31	6.32	6.33
E-plane HPBW	74.8°	74.7°	74.5°	74.4°
H-plane HPBW	134.0°	134.2°	134.3°	134.0°
Radiation efficiency (%)	84.22	85.06	86.42	86.53
FTBR (dB)	21.5	21.7	22.0	21.8

APPENDIX II. FOUR ELEMENT INFINITESIMAL DIPOLE ARRAY MODEL

We have found that a four-element dipole array model properly describes the far-field response of the slot-modified disc-augmented EAD antenna system. Fig. 7 shows this model. All of the dipoles are oriented parallel to the z-axis. Referring to Fig. 1, both Ant_1 and Ant_2 are located at a distance h from the origin along the x-axis. Antennas Ant_3 and Ant_4 are located at a distance d from the origin along the y-axis. These choices conform to the coordinate axes shown in Fig. 2(a). As explained in Section III, the elements labeled Ant_1 and Ant_2 correspond, respectively, to the active element and its image in the parasitic disc; Ant_3 and Ant_4 arise from the meanderline slots cut in it. In exciting each of the four dipoles in this analytical model, the amplitude and phase of Ant_1 are taken to be the reference values. Its amplitude is set to 1.0; its phase is set to 0°. Ant_2 is excited with π phase difference, i.e., it has an out-of-phase excitation, and an amplitude A. We consider Ant_3 and Ant_4 to be excited in-phase with the same phase difference (π-β) with respect

to the reference value and with the same amplitude B. All of these infinitesimal dipoles operate in a fundamental dipole mode. Thus, their respective E-field components can be written in far-field region as [18]

$$\vec{E}_{far\ field} = jk\eta I_0 \ell \frac{e^{-jkr}}{4\pi r} \sin\theta\widehat{\theta} \tag{A1}$$

$$E_r^{far\ field} = E_\phi^{far\ field} = 0. \tag{A2}$$

Using the basic principles of pattern analysis [18], the normalized directivity patterns of this four-element dipole antenna system can be obtained from the expressions.

In the XZ-plane (i.e., in E-plane)

$$D_E \propto \left\{ \begin{array}{l} [(1-A)\cos(kh\sin\theta) - 2B\cos\beta]^2 \\ +[(1+A)\sin(kh\sin\theta) + 2B\sin\beta]^2 \end{array} \right\} \times \sin^2\theta \tag{A3}$$

and in the XY-plane (i.e., in H-plane)

$$D_H \propto [(1-A)\cos(kh\cos\phi) - 2B\cos(kd\sin\phi)\cos\beta]^2 + [(1+A)\sin(kh\cos\phi) + 2B\cos(kd\sin\phi)\sin\beta]^2. \tag{A4}$$

Our interest is to see whether or not such an arrangement of antennas can produce the observed high directivity along the x-axis and FTBR values, i.e., very small power flow, along the $-x$-axis. This is achieved by suitably arranging the magnitudes (A and B) and phases (β) of the array elements. Note that because our final design is meant to be electrically small, both $2h$ and $2d$ are taken to be less than $0.3\lambda_0$. Since we are treating them as ideal elements, the explicit mutual interactions between the array elements are not a concern, even in such a dense configuration.

As an example, consider one of the optimal cases, which occurs for the parameter values: $h = 0.1\lambda_0$, and $d = 0.15\lambda_0$. Varying the amplitude and phase parameters, the optimized E- and H-plane normalized directivity patterns are shown in Fig. 15(a) for the case with $A = 0.15$, $B = 0.45$, $\beta = \pi/4$. One observes that the desired cardioid pattern is obtained, with the more than a 25 dB FTBR. This $\pi/4$ phase difference between each element and the reference is what led to the quarter-wavelength long design of the meanderline slots. To understand the mutual coupling effects, the same array was simulated with HFSS. The radius and length of each dipole was, respectively, $0.0005\lambda_0$ and $0.1\lambda_0$; each element was impedance matched to its stand-alone value. The magnitudes and phases were then varied to obtain an optimal directivity behavior. The optimized results are presented in Fig. 15(b) for comparison. A 6.34 dB peak directivity and a 22.47 dB front-to-back ratio were obtained. Clearly, the mutual coupling impacts both values; but the FTBR value is commensurate with the analytical model result.

To clarify further the importance of the second two-element sub-array, Ant_3 and Ant_4, the radiation patterns of this two-element sub-array and the entire four-element array were obtained with the analytical model by varying the separation distance $2d$ between Ant_3 and Ant_4. Fig. 16 shows the

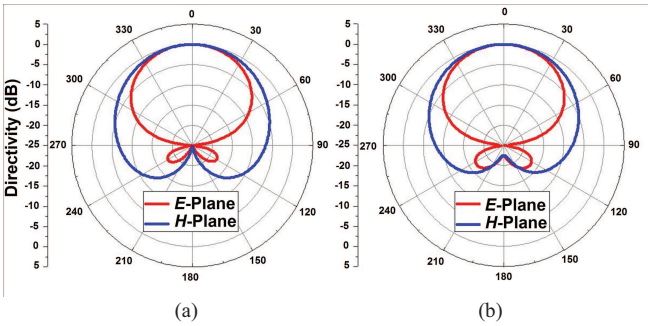

FIGURE 15. Simulated *E*- and *H*-plane directivity patterns obtained for the four-element dipole array. (a) Analytical model with $A = 0.15$, $B = 0.45$, $\beta = \pi/4$; and (b) HFSS model with $A = 0.1$, $B = 0.25$, $\beta = \pi/3$.

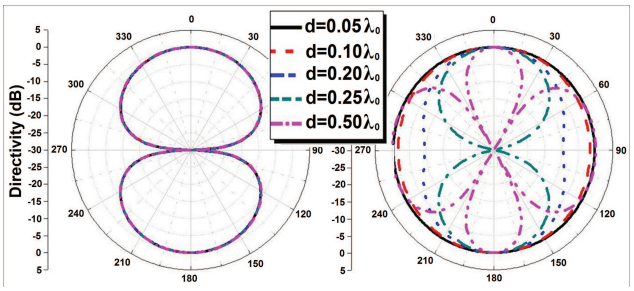

FIGURE 16. Normalized radiation patterns of an in-phase, two-element dipole array with $2d$ being their distance of separation. (a) *E*-plane, and (b) *H*-plane.

effects of $2d$ on the radiation patterns of a two-dipole array in which the elements are parallel and excited in-phase with the same amplitude. It is observed that if the separation distance $2d$ is less than $2 \times 0.2\lambda_0$, the array produces a nearly omnidirectional radiation pattern in the H-plane. In contrast, when the distance is larger than $2 \times 0.2\lambda_0$, there is significant degradation of this behavior. In our parameter studies of the lengths and shapes of the meanderline slots, it was observed that variations in them had little impact on the H-plane pattern results as long as d maintained the electrical smallness of the system, i.e., $d < 0.15\lambda_0$. This behavior was advantageous for our final designs since varying the slot shapes and sizes then had a minimal effect on the H-plane patterns. Similarly, the impact of changing the distance d of the sub-array on the radiation patterns of the four element array was studied. As shown in Fig. 17, while the E-plane patterns remain the same, the smallest values of d lead to the smallest back radiation values and the widest half-power beamwidth (HPBW) values in the H-plane patterns.

These results suggested to us that the presence of three parasitic elements, which became the conducting disc and the two meanderline slots placed in the near-field of a driven ESA, could produce the desired directivity and FTBR behaviors. When the ESA is excited, these parasitic structures would be naturally excited through the strong near-field mutual coupling effects. The resonant parasitic elements would then re-radiate, acting as three additional "effective"

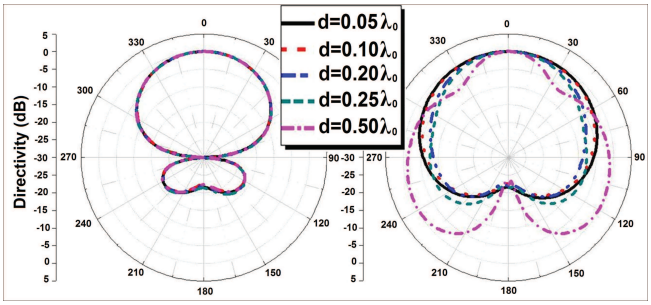

FIGURE 17. Normalized radiation patterns of the four-element dipole array as the separation distance, *2d*, between Ant_3 and Ant_4 is varied. (a) *E*-plane, and (b) *H*-plane.

antennas. Thus, as was done with the analytical model, we investigated how to adjust the mutual coupling level, for instance, by changing the distances between and the sizes of the parasitic structures in the actual antenna to obtain the amplitudes and phases that would generate the desired radiation pattern behaviors.

The actual design of the resonant slot-modified parasitic disc required much effort. Its evolution is shown in Fig. 18. The first issue faced was how to feed the EAD antenna in the presence of a copper disc. Since a practical EAD antenna had been verified with a coax feedline [12], this feed structure was chosen. This meant a coax had to be inserted through the parasitic disc. The natural location of the coax feedline was always taken to be at the center of the disc, since, as shown above, the excitation of the two meanderline slots needed to be symmetrical. Two versions were tried: the copper disc being connected to the outer wall of the coax, and the copper disc being a parasitic, the centered hole being larger than the outer wall diameter of the coax to avoid shorting it.

It was found immediately that shorting the disc destroyed the ability of the current distributions associated with the slots to have different phases relative to the image of the active element. The four-element array thus lost its ability to create the necessary phased superpositions. As a consequence, our designs proceeded with an annular slot around the coax feed. In effect, the slot-modified parasitic copper disc becomes a parasitic element in the near field of the EAD antenna. This step in the process is the second diagram shown in Fig. 18.

Through the HFSS simulations, it became understood that the currents near the interior ends of the slots played a major role in overall behavior of the system, notably the FTBR. Consequently, we also investigated how to control those currents locally by modifying the shape of the ends of the slots. This part of the design process is shown in the third subplot of Fig. 18. Finally, simulations showed that straight slots which were on the order of a quarter wavelength long were sufficient to obtain the desired phase relationships between the currents on the parasitic disc and the EAD to generate the desired cardioid pattern results. However, this strictly violated our electrically small criterion. It was found then that by meandering the slot, we could obtain the necessary quarter-

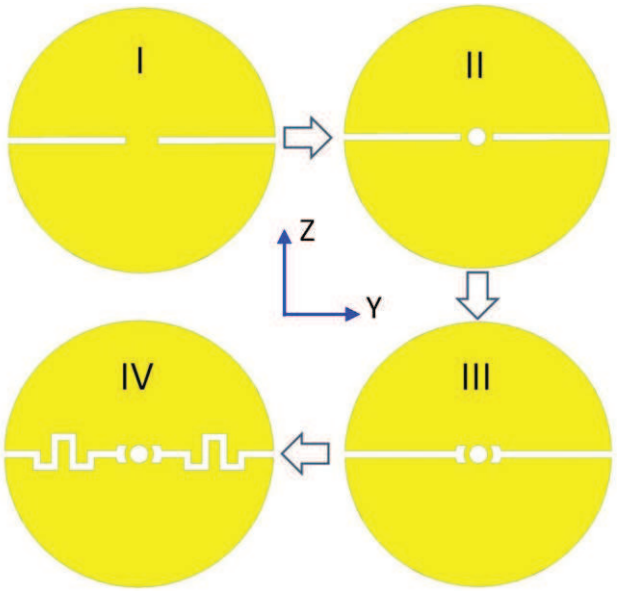

FIGURE 18. Evolution of the design of the slots in the parasitic copper disc.

wavelength length in a small region. This is depicted by the fourth subfigure in Fig. 18.

We note that slots whose ends did not go to the edge of the parasitic copper disc were also tried. It was found that if the exterior edge of the disc was not cut by the slot, the currents did not flow properly on it. It was decided to use two symmetrical tapers at the interior ends of the slots that conformed to the circular shape of the annular slot to obtain smooth current transitions from along the z-axis to those along the y-axis. They were tuned by investigating the width of the tapers, their angular extent and the distances between the taper and the annular hole. These parameters allowed us to adjust the coupling between the slots and the EAD antenna and its image and, hence, to control the current strengths and phases. Deeper slot variations away from the y-axis were examined, as well as more periods in the meandering slot. It was found that the radiation efficiency was the best with the fewest number of corners, i.e., the fewest number of periods, and the shallowest variations away from the y-axis. The quarter-wavelength length of the slots caused the total effective length of the current paths to be a half-wavelength. The resulting relative phases caused the currents induced on the front and back sides of the parasitic disc to be the same, which was necessary to achieve the desired cardioid-like results. We note that if a larger ground plane with two straight quarter-wavelength slots were allowed, significantly larger FTBRs (greater than 30 dB) have been obtained.

REFERENCES

[1] J. Joubert, J. C. Vardaxoglou, W. G. Whittow, and J. W. Odendaal, "CPW-Fed cavity-backed slot radiator loaded with an AMC reflector," *IEEE Trans. Antennas Propag.*, vol. 60, no. 2, pp. 735–742, Feb. 2012.

[2] R. Baggen, M. Martínez-Vázquez, J. Leiss, S. Holzwarth, L. Salghetti Drioli, and P. de Maagt, "Low profile GALILEO antenna using EBG technology," *IEEE Trans. Antennas Propag.*, vol. 56, no. 3, pp. 667–674, Mar. 2008.

[3] A. A. Roseline, K. Malathi, and A. K. Shrivastav, "Enhanced performance of a patch antenna using spiral-shaped electromagnetic bandgap structures for high-speed wireless networks," *IET Microw., Antennas Propag.*, vol. 5, no. 14, pp. 1750–1755, Nov. 2011.
[4] G. Mumcu, K. Sertel, and J. L. Volakis, "Miniature antenna using printed coupled lines emulating degenerate band edge crystals," *IEEE Trans. Antennas Propag.*, vol. 57, no. 6, pp. 1618–1624, Jun. 2009.
[5] E. E. Altshuler, T. H. O'Donnell, A. D. Yaghjian, and S. R. Best, "A monopole superdirective array," *IEEE Antennas Propag.*, vol. 53, no. 8, pp. 2653–2661, Aug. 2005.
[6] S. Lim and H. Ling, "Design of electrically small Yagi antenna," *Electron. Lett.*, vol. 43, no. 5, pp. 3–4, Mar. 2007.
[7] A. D. Yaghjian, T. H. O'Donnell, E. E. Altshuler, and S. R. Best, "Electrically small supergain end-fire arrays," *Radio Sci.*, vol. 43, no. 3, article no. RS3002, Jun. 2008.
[8] I.-J. Yoon and H. Ling, "An electrically small Yagi antenna with enhanced bandwidth characteristics using folded cylindrical helix dipoles," *Microw. Opt. Technol. Lett.*, vol. 53, no. 6, pp. 1231–1233, Jun. 2011.
[9] ANSYS Corp. (2012). *ANSYS/ANSOFT High Frequency Structure Simulation (HFSS), ver. 13.0* [Online]. Available: www.ansoft.com
[10] (2013). *CST Microwave Studio, CST of America, Inc* [Online]. Available: http://www.cst.com
[11] P. Jin and R. W. Ziolkowski, "Metamaterial-inspired, electrically small, Huygens sources," *IEEE Antennas Wireless Propag. Lett.*, vol. 9, no. 5, pp. 501–505, May 2010.
[12] R. W. Ziolkowski, P. Jin, and C.-C. Lin, "Metamaterial-inspired engineering of antennas," *Proc. IEEE*, vol. 99, no. 10, pp. 1720–1731, Oct. 2011.
[13] P. Jin, C.-C. Lin, and R. W. Ziolkowski, "Multi-functional, electrically small, planar near-field resonant parasitic antennas," *IEEE Antennas Wireless Propag. Lett.*, vol. 11, no. 3, pp. 200–204, Mar. 2012.
[14] P. Jin and R. W. Ziolkowski, "High directivity, electrically small, low-profile, near-field resonant parasitic antennas," *IEEE Antennas Wireless Propag. Lett.*, vol. 11, no. 4, pp. 305–309, Apr. 2012.
[15] N. Zhu and R. W. Ziolkowski, "Active metamaterial-inspired broad-bandwidth, efficient, electrically small antennas," *IEEE Antennas Wireless Propag. Lett.*, vol. 10, no. 2, pp. 1582–1585, Feb. 2011.
[16] N. Zhu and R. W. Ziolkowski, "Broad bandwidth, electrically small antenna augmented with an internal non-Foster element," *IEEE Antennas Wireless Propag. Lett.*, vol. 11, no. 10, pp. 1116–1120, Oct. 2012.
[17] W.-G. Lim, H.-S. Jang, and J.-W. Yu, "New method for back lobe suppression of microstrip patch antenna for GPS," in *Proc. 40th Eur. Microw. Conf.*, Sep. 2010, pp. 679–682.
[18] C. A. Balanis, *Antenna Theory: Analysis and Design*, 3rd ed. New York, NY, USA: Wiley, 2005.

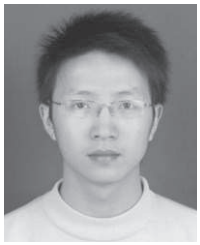

MING-CHUN TANG (S'12) received the B.S. degree in physics from Neijiang Normal University, Neijiang, China, in 2005. He is currently pursuing the Ph.D. degree in radio physics with the University of Electronic Science and Technology of China, Chengdu, China, since 2007. From August 2011 to August 2012, he is with the Department of Electrical and Computer Engineering, The University of Arizona, Tucson, AZ, USA, as a Visiting Scholar.

He is the recipient of Best Student Paper Award in 2010 International Symposium on Signals, Systems and Electronics (ISSSE'2010), Nanjing, China. He is serving as a reviewer for IEEE journals, including the IEEE Antennas and Wireless Propagation Letters and the IEEE *Antennas and Propagation Magazine*. His current research interests include miniature antenna, RF circuit, metamaterial design, and its application.

RICHARD W. ZIOLKOWSKI (M'97–SM'91–F'94) received the B.Sc. degree (Hons.) in physics (*magna cum laude*) from Brown University, Providence, RI, USA, in 1974, the M.S. and Ph.D. degrees in physics from the University of Illinois at Urbana-Champaign, Urbana, IL, USA, in 1975 and 1980, respectively. He was awarded an Honorary Doctorate, *Doctor Technish Honoris Causa*, from the Technical University of Denmark in 2012. He was a member of the Engineering Research Division, Lawrence Livermore National Laboratory from 1981 to 1990 and served as the Leader of the Computational Electronics and Electromagnetics Thrust Area for the Engineering Directorate. He currently is serving as the Litton Industries John M. Leonis Distinguished Professor with the Department of Electrical and Computer Engineering, University of Arizona, Tucson, AZ, USA. He holds a joint appointment with the College of Optical Sciences. He is an OSA fellow. He was the President of the IEEE Antennas and Propagation Society in 2005. He continues to be very active in the IEEE, OSA, and APS professional societies. His current research interests include the application of new physics and engineering ideas to linear and nonlinear problems dealing with the interaction of electromagnetic waves with complex media, metamaterials, and realistic structures.